Eur. Phys. J. D **22**, 401–415 (2003)
DOI: 10.1140/epjd/e2003-00017-9

THE EUROPEAN PHYSICAL JOURNAL D

Nondispersive two-electron wave packets in driven helium

P. Schlagheck[1] and A. Buchleitner[2,a]

[1] Institut für Theoretische Physik, Universität Regensburg, 93040 Regensburg, Germany
[2] Max-Planck-Institut für Physik komplexer Systeme, Nöthnitzer Str. 38, 01187 Dresden, Germany

Received 7 November 2002 / Received in final form 2 December 2002
Published online 28 January 2003 –

Abstract. We provide a detailed quantum treatment of the spectral characteristics and of the dynamics of nondispersive two-electron wave packets along the periodically driven, collinear frozen planet configuration of helium. These highly correlated, long-lived wave packets arise as a quantum manifestation of regular islands in a mixed classical phase space, which are induced by nonlinear resonances between the external driving and the unperturbed dynamics of the frozen-planet configuration. Particular emphasis is given to the dependence of the ionization rates of the wave packet states on the driving field parameters and on the quantum mechanical phase space resolution, preceded by a comparison of 1D and 3D life times of the unperturbed frozen planet. Furthermore, we study the effect of a superimposed static electric field component, which, on the grounds of classical considerations, is expected to stabilize the real 3D dynamics against large (and possibly ionizing) deviations from collinearity.

PACS. 32.80.Rm Multiphoton ionization and excitation to highly excited states (e.g., Rydberg states) – 05.45.Mt Semiclassical chaos ("quantum chaos") – 31.25.Jf Electron correlation calculations for atoms and ions: excited states

1 Introduction

As documented by an increasing amount of literature, electronic wave packets represent an important object of experimental studies in atomic and molecular physics (*e.g.*, [1,2]). The possibility to localize the electronic population in phase space can be regarded as the crucial link between a quantum wavefunction and a classical point particle [3], and has led to various applications in the context of quantum control (*e.g.*, [4,5]). For a long time, it was common belief that the maximum evolution time until which such a localized phase space distribution can be maintained is ultimately limited by the time scale corresponding to the anharmonicity of the underlying classical potential. After this time scale, any coherent superposition which was initially well localized in position and momentum space would have spread out over the whole classical orbit due to dispersion, *i.e.*, due to the fact that different components of the superposition contribute with different classical frequencies. This is usually termed as the *collapse* of the wave packet.

A decade ago, however, it was found that this spreading can actually be suppressed by means which are common in quantum control, namely by applying electromagnetic fields to the quantum configuration. This was explicitly demonstrated for one-electron atoms driven by microwave fields with linear [6–8], circular [9,10], and elliptic polarization [11]. There, a Rydberg wave packet, initially launched along a Kepler orbit with principal quantum number n, is exposed to a microwave field which is resonant with the periodic classical motion. Then, for appropriate field amplitudes (which must neither be too strong nor too weak, compared to the Coulomb force on the electron) and for the appropriate relative phase between the microwave field and the Kepler oscillation, the spreading of the wave packet (which usually occurs after approx. $n/[3\pi(\Delta n)^2]$ Kepler cycles, given a coherent superposition of Δn unperturbed eigenstates centered around n) is *completely inhibited*. While perfectly keeping their shape, such *nondispersive wave packets* may well follow the classical motion over time scales up to 10^6 Kepler cycles [6,8,10,12] before appreciable ionization (induced by the driving field) sets in [6,8,13]. This stabilization phenomenon is best understood from the underlying classical dynamics. In classical phase space, the time-periodic perturbation of the microwave destroys the global integrability of the Coulomb dynamics; local "islands" of regular motion, embedded into a "sea" of chaotic, ionizing dynamics, are created by the nonlinear resonance between the driving field and the unperturbed Kepler motion. The nondispersive quantum wave packets are nothing but the time-periodic eigenstates (Floquet states) of the driven atom, which arise from a local quantization within these resonance islands [14,15] (see [16] for a recent review on the topic).

[a] e-mail: abu@mpipks-dresden.mpg.de

The above interpretation in terms of nonlinear resonances in a mixed phase space suggests that the concept of nondispersive wave packets can be generalized to atomic (or molecular) systems that are more complex than hydrogen or hydrogen-like Rydberg atoms – such as, *e.g.*, the correlated dynamics in doubly excited helium. However, such a generalization is not at all obvious, since most doubly excited two-electron orbits of the bare three-body Coulomb problem (as the classical version of the doubly excited helium atom) are unstable and promote rapid autoionization of the configuration. This prevents the confinement of an initially localized wave packet on longer time scales.

Nonetheless, extensive studies on the classical dynamics of helium [17] have identified local regions of regular motion which are associated with configurations of particular symmetry of the two-electron atom. The most prominent and surprising example is the "frozen planet" orbit [18,19], a highly polarized, nearly collinear configuration with asymmetric excitations of the electrons. The frozen planet's stability essentially relies on the nonnegligible electron-electron interaction (the electrons are, contrary to intuition, located on the *same* side of the nucleus). Stable eigenmodes sustain radial, vibration-like oscillations of the outer electron, as well as coupled transverse excursions of the outer and inner electron. Well-defined eigenfrequencies are associated with these eigenmodes, what makes the configuration a good candidate for inducing nonspreading wave packets in the correlated two-electron dynamics, by near-resonant external driving.

In fact, our earlier analysis of the classical dynamics of helium in a linearly polarized electromagnetic field already provided strong support for nondispersive wave packets along the frozen-planet orbit [20,21]. The external perturbation induces regular islands within the phase space of collinear motion (where electrons and nucleus are lined up parallel to the driving field polarization axis), which are due to nonlinear resonances between the drive and the oscillation of the outer electron. The dynamics within these resonances is in general unstable with respect to deviations from collinearity (in contrast to the analogous scenario in atomic hydrogen, the resonantly driven one dimensional Kepler orbit [22]). However, a static electric field applied parallel to the microwave polarization axis can be used to enforce stability of the driven configuration in all three spatial dimensions [20]. This suggests that nondispersive two-electron wave packets can be built on these stabilized resonances, and, on the basis of semiclassical considerations, at experimentally accessible quantum numbers of doubly excited helium [21,23]. Yet, this conjecture remains to be corroborated by an exact quantum treatment.

With the presently available computational facilities, full blown quantum *ab initio* calculations of highly correlated two-electron wave packet states under electromagnetic driving are prohibitive. However, since the stabilizing static field confines the wave packet to the near vicinity of the field polarization axis, essential properties of these wave packets appear accessible through the restriction of the quantum dynamics along this axis. Indeed, nondispersive two-electron wave packets associated with the classical resonances are found in quantum calculations on the collinear model atom, as we have already reported in a previous letter [24]. Here we shall give detailed account of our quantum treatment of these objects, identify them as special eigenstates in the Floquet spectrum of the driven atomic system (alike their counterparts in driven hydrogen atoms), and investigate their characteristic properties.

To make the present contribution self-contained, we start out in Section 2 with a review of the classical dynamics of the driven frozen-planet configuration, which was already described elsewhere [20,21]. Section 3 is devoted to the formulation of the quantum eigenvalue problem for the collinear model. As a first application thereof, we study the unperturbed collinear atom in Section 4, what provides a remarkable example of regular dynamics in an atomic two-electron system. In Section 5, we show how the nondispersive wave packets emerge in the spectrum of driven helium (Sect. 5.1) and discuss their lifetimes (Sect. 5.2), as well as their properties in presence of an additional static electric field (Sect. 5.3).

2 Classical dynamics of the driven frozen-planet configuration

2.1 The frozen-planet configuration of helium

In atomic units, which are used throughout this paper, the classical Hamiltonian of the electromagnetically driven helium atom reads

$$H = \frac{\mathbf{p}_1^2}{2} + \frac{\mathbf{p}_2^2}{2} - \frac{Z}{|\mathbf{r}_1|} - \frac{Z}{|\mathbf{r}_2|} + \frac{1}{|\mathbf{r}_1 - \mathbf{r}_2|} + \mathbf{F}(t)\,(\mathbf{r}_1 + \mathbf{r}_2), \tag{1}$$

with $\mathbf{r}_i = (x_i, y_i, z_i)$ and $\mathbf{p}_i = (p_{ix}, p_{iy}, p_{iz})$ the position and the momentum of electron $i = 1, 2$, respectively, $Z = 2$ the nuclear charge, and

$$\mathbf{F} = (F \cos \omega t + F_{\rm st})\,\mathbf{e}_z \tag{2}$$

the external, linearly polarized driving at frequency ω and amplitude F, possibly superimposed by an additional, static component with field strength $F_{\rm st}$ ($\mathbf{e}_z$ represents the unit vector along the z-axis). In analogy to driven hydrogen [25] as well as to the unperturbed helium atom [26], the Hamiltonian (1) exhibits general scaling laws: the classical dynamics generated by (1) remain invariant if all variables and parameters of the system are transformed according to

$$\begin{aligned} \mathbf{r}_i &\longmapsto N^2\,\mathbf{r}_i \quad (i = 1, 2), \\ \mathbf{p}_i &\longmapsto N^{-1}\,\mathbf{p}_i \quad (i = 1, 2), \\ t &\longmapsto N^3\,t, \\ \mathbf{F} &\longmapsto N^{-4}\,F, \\ \omega &\longmapsto N^{-3}\,\omega, \\ H &\longmapsto N^{-2}\,H, \end{aligned} \tag{3}$$

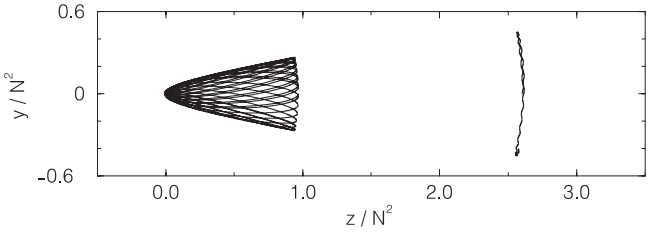

Fig. 1. A typical (planar) trajectory of the frozen-planet configuration. While the inner electron oscillates on eccentric Kepler trajectories around the nucleus, the outer electron is dynamically stabilized and remains nearly "frozen" around a given equilibrium distance. The configuration is stable against autoionization and represents a large regular region in the classical phase space of helium.

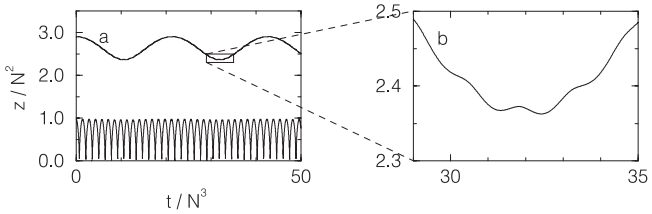

Fig. 2. Collinear trajectory of the frozen-planet configuration. The positions of the electrons are plotted as a function of time. We see that the dynamics is characterized by two almost separable modes: (i) the Kepler mode of the inner electron, which also manifests in the motion of the outer electron, as shown in the magnification (b) of the latter's trajectory; (ii) the slow oscillation of the outer electron around the equilibrium distance, which induces a feeble (and, at this scale, hardly visible) modulation of the amplitude of the inner electron's excursion.

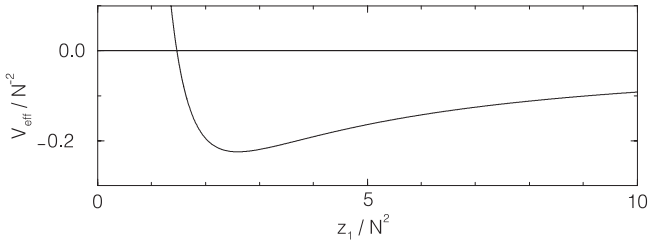

Fig. 3. Effective adiabatic potential describing the slow oscillation of the outer electron around its equilibrium position (see [28]). Intrinsic scales for frequency and field strength can be inferred from the shape of the potential. The natural scale of the field strength, $F_I \simeq 0.03\,N^{-4}$, is given by the maximum slope of the potential (at $z_1 \simeq 3.7\,N^2$). The frequency scale, $\omega_I \simeq 0.3\,N^{-3}$, is given by the curvature of the potential at its minimum at $z_1 \simeq 2.6\,N^2$, *i.e.*, by the frequency of small oscillations around the equilibrium.

where N represents an arbitrary, real positive quantity. Since any classical action scales linearly with N (as does the product of position and momentum), we shall identify N with the principal quantum number of the inner electron, which corresponds to the action variable of its Kepler orbit. Due to the above scale invariance, we can restrict our classical phase space analysis to a fixed quantum number $N = 1$, and use (3) to deduce the actual phase space structure of the energy range of interest.

Figure 1 shows a solution of the classical equations of motion generated by (1), which illustrates the frozen planet configuration we shall focus on throughout this paper. Both electrons are located on the *same* side of the nucleus, librating with respect to a common symmetry axis. While the inner electron oscillates on extremely eccentric Kepler trajectories around the nucleus, the outer electron is dynamically stabilized due to the rapid oscillation of the inner, and remains nearly "frozen" in the vicinity of an equilibrium distance where the attractive and repulsive forces due to the other charged particles cancel each other when averaged over one Kepler cycle of the inner electron. The configuration is *classically stable* against autoionization and defines a relatively large region of regular motion in the dominantly chaotic phase space of helium. Exact quantum calculations on doubly excited helium [19] have indeed revealed the existence of long-lived autoionizing states (of which the energetically lowest one lies below the $N = 3$ threshold) which are localized along the frozen-planet orbit.

For a suitable choice of initial conditions, the motion of the electrons remains confined to the z-axis, what defines the subspace of collinear motion. In this simplest case, the regular frozen-planet dynamics is characterized by two modes which almost perfectly separate (Fig. 2): the fast Kepler mode of the inner electron (which is also manifest in the motion of the outer electron, see Fig. 2b) and the slow oscillation of the outer electron around the equilibrium distance (which also affects the motion of the inner electron, as a slow modulation of its maximal excursion).

This separation of time scales (the Kepler oscillation is almost 15 times faster than the slow mode of the outer electron) allows to treat the frozen-planet dynamics within the formalism of adiabatic invariants [27]. This defines an effective potential which describes the slow dynamics of the outer electron, in the combined field of the nucleus and of the rapidly oscillating inner electron [28]. As we see in Figure 3, this potential is attractive Coulombic for large distances (due to the attraction by the nucleus), strongly repulsive for short distances (due to encounter with the inner electron) and exhibits a local minimum at the equilibrium distance.

From the shape of this potential, we can immediately infer intrinsic scales for the frequency and the field strength, which depend only on the inner electron's quantum number N, and which completely determine the effect of an external drive on the configuration. The natural scale for the field strength, $F_I \simeq 0.03\,N^{-4}$, is given by the maximum slope of the potential (at $z_1 \simeq 3.7\,N^2$; throughout the paper, subscript 1 denotes the outer, and subscript 2 the inner electron), and indicates the maximum static field that can be applied to the configuration without ionizing it. The frequency scale $\omega_I \simeq 0.3\,N^{-3}$ is given by the curvature of the potential at its minimum, *i.e.*, by the frequency of small oscillations around the equilibrium position. In the following, we shall study the effect of an electromagnetic field which *resonantly* drives

the outer electron's slow oscillation, *i.e.*, a field with amplitude $F < F_I$ and frequency $\omega \simeq \omega_I$.

2.2 Phase space of the collinear, driven configuration

In the presence of the time-periodic perturbation, the dynamics of the collinear, driven frozen-planet evolves in a five-dimensional phase space spanned by the positions and momenta of the electrons, and by the phase ωt of the driving field. A complete visualization of the driven dynamics within a simple two-dimensional Poincaré surface of section is therefore not possible. However, for $\omega \simeq \omega_I$, and for field amplitudes $F < F_I$ which do not appreciably affect the Kepler motion of the inner electron, the separation of time scales allows to map the phase space structure onto a two-dimensional surface by means of a two-step Poincaré section method [21,23]. We begin with a simple Poincaré section by plotting the outer electron's phase space variables z_1, p_{z1} whenever the inner electron reaches the nucleus ($z_2 = 0$) – *i.e.*, whenever the phase of the Kepler oscillation assumes a fixed value. In the time domain, the points obtained by this section are separated by the Kepler period which is much shorter than any other time scale in the system. The dynamics generated by the *slow* modes – *i.e.*, the outer electron's oscillation within the effective potential, as well as the external driving – is therefore very well monitored by this sequence of points.

Neglecting the effect of resonances between fast and slow dynamics, the intersection of the Lagrangian manifold with the surface defined by $z_2 = 0$ can now be very well approximated by a cubic interpolation between subsequent points in the above sequence. This yields a *continuous* trajectory which can be used to perform a second Poincaré section, by fixing the phase of the driving field $\omega t = \phi_0 \pmod{2\pi}$. As a consequence, we effectively plot the outer electron's position and momentum for $z_2 = 0$ and for fixed ωt. The reduction of the phase space to a two-dimensional surface is completed by restricting the initial conditions to those with fixed value $N = 1$ of the inner electron's action. This latter quantity represents an adiabatic invariant of the system and therefore remains nearly constant as time evolves.

Figure 4 shows the Poincaré section that is obtained by the two-step method described above, for fixed frequency $\omega = 0.2\,N^{-3} < \omega_I$, fixed driving phase $\omega t = 0$, and for variable field amplitude F. In the unperturbed case ($F = 0$, Fig. 4a), we recognize a regular phase space structure, with closed curves corresponding to the regular oscillation of the outer electron within the effective potential. If we switch on the driving field, phase space turns mixed regular-chaotic. The bounded frozen-planet dynamics is now represented by a local regular region centered around the equilibrium point, outside which the dynamics is chaotic and leads to ionization. This remaining regular region is, due to the Kolmogorov-Arnold-Moser (KAM) theorem [27], still large for weak field amplitudes ($F = 0.001\,N^{-4}$, Fig. 4b), but decreases in size with increasing F. As a consequence of the Poincaré-Birkhoff theorem [27], elliptic substructures, induced by nonlinear

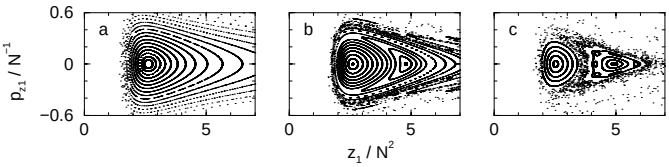

Fig. 4. Phase space of the collinear, driven frozen-planet configuration, for variable field amplitudes, (a) $F = 0$, (b) $0.001\,N^{-4}$, (c) $0.005\,N^{-4}$, at fixed driving frequency $\omega = 0.2\,N^{-3}$. The momentum p_{z1} of the outer electron is plotted *versus* its position z_1 at fixed action $N = 1$ of the Kepler mode, fixed position $z_2 = 0$ of the inner electron, and fixed phase $\omega t = 0 \pmod{2\pi}$ of the driving field [21,23]. The regular phase space of the unperturbed atom (a) turns mixed regular-chaotic in presence of the external perturbation (b, c). The nonlinear 1:1 resonance between the driving field and the unperturbed oscillation of the electron gives rise to a substructure at $F = 0.001\,N^{-4}$ (b) (centered around $z_1 \simeq 4.8\,N^2$), which transforms into a separate regular island within the chaotic sea at larger field amplitude $F = 0.005\,N^{-4}$ (c).

resonances between the external driving and the unperturbed oscillation of the outer electron, emerge within the regular region. The prominent substructure located around $z_1 \simeq 4.8\,N^2$ for $F = 0.001\,N^{-4}$ (Fig. 4b) corresponds to the 1:1 resonance where one oscillation cycle of the outer electron is completed after precisely one period of the driving field.

At larger field amplitude ($F \simeq 0.003\,N^{-4}$ for the frequency used in Fig. 4), the field-induced resonance eventually disconnects from the rest of the regular domain. The phase space then exhibits two separate, large regular islands embedded into the chaotic sea (see Fig. 4c at $F = 0.005\,N^{-4}$): the *intrinsic* island (centered around $z_1 \simeq 2.5\,N^2$ in Fig. 4c) which is essentially due to the intrinsic nonlinear frozen-planet dynamics with the external field acting only as a small perturbation, and the field-induced *1:1 resonance* island (centered around $z_1 \simeq 4.9\,N^2$ in Fig. 4c) which arises from the combination of two equally important nonlinear components: the coupling to the external driving field and the internal interactions between the charged particles of the atom.

Figure 5 illustrates the effect of tuning the frequency ω at fixed field amplitude $F = 0.005\,N^{-4}$. With increasing ω, the field-induced resonance shifts towards lower excitations within the effective potential, *i.e.*, towards unperturbed orbits with higher frequencies. Consequently, the resonance island is located closer (as compared to Fig. 4c) to the equilibrium distance for $\omega = 0.25\,N^{-3}$ (Fig. 5a) and finally undergoes a smooth transition into the intrinsic island at $\omega = 0.3\,N^{-3} \simeq \omega_I$ (Fig. 5b). Above the intrinsic frequency ω_I – which corresponds to the maximum frequency of free oscillations within the effective potential – the electromagnetic field can no longer induce a 1:1 resonance. Resonances of higher order, however, are still possible (*e.g.*, the 2:1 resonance, where one period of the outer electron is completed precisely after two field cycles; the elliptic islands created by this resonance are located at $z_1 \simeq 4\,N^2$ and $p_{z1} \simeq \pm 0.2\,N^{-1}$ in Fig. 5c).

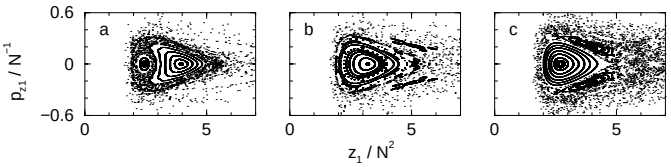

Fig. 5. Phase space of the collinear, driven frozen planet configuration for variable driving frequency, (a) $\omega = 0.25\,N^{-3}$, (b) $0.3\,N^{-3}$, (c) $0.4\,N^{-3}$, at fixed amplitude $F = 0.005\,N^{-4}$ and phase $\omega t = 0$ of the drive. With increasing ω, the 1:1 resonance island (centered around $z_1 \simeq 3.9\,N^2$ in (a)) shifts towards the equilibrium distance, and finally undergoes a smooth transition into the intrinsic island at $\omega = \omega_I = 0.3\,N^{-3}$ (b). The two islands at $z_1 \simeq 4\,N^2$, $p_{z1} \simeq \pm 0.2\,N^{-1}$ for $\omega = 0.4\,N^{-3}$ (c) are induced by the 2:1 resonance where one period of the outer electron's motion matches two field cycles.

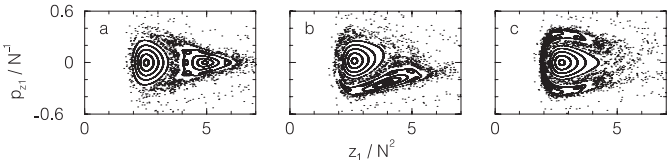

Fig. 6. Phase space of the collinear, driven configuration for variable phases of the driving field, (a) $\omega t = 0$, (b) $\pi/2$, (c) π, at fixed frequency $\omega = 0.2\,N^{-3}$ and field amplitude $F = 0.005$. While the intrinsic island remains basically at rest during time evolution, the field-induced 1:1 resonance island faithfully traces the resonantly driven trajectory of the outer electron.

The crucial qualitative difference between the intrinsic island and the field-induced resonances is best illustrated by visualizing the phase space structure for different times, *i.e.*, by performing the above two-step Poincaré section for different phases ωt of the driving field. Figure 6 shows the phase space of the driven configuration at $\omega = 0.2\,N^{-3}$, $F = 0.005\,N^{-4}$, for the field phases $\omega t = 0$, $\pi/2$, and π. We see that the intrinsic island remains basically at rest during the time evolution. The field-induced 1:1 resonance island, on the other hand, oscillates once around the intrinsic island within one field cycle.

2.3 Stabilization against deviations from collinearity

In contrast to their counterparts in driven hydrogen [16,29], however, the resonance islands of the collinear, driven frozen-planet dynamics are *not* embedded in a regular phase space domain of the three-dimensional problem. Figure 7 shows the evolution of the configuration launched at the center of the 1:1 resonance island of Figure 5a (*i.e.*, for $\omega = 0.25\,N^{-3}$ and $F = 0.005\,N^{-4}$) if the outer electron is slightly displaced from collinearity by a small transverse component $y_1 = 0.01\,N^2$ of its position. Due to the effective torque exerted by the driving field on the configuration, the initially small deviation from the field polarization axis increases rapidly with time, until, after about ten field cycles, both electrons "flip over" to the other side of the nucleus. The configuration then performs several chaotic rotations around the center, until the correlation between the electrons eventually breaks down and the atom ionizes after a subsequent electron-electron collision. This transverse instability turns out to be characteristic not only for the 1:1 resonance, but also for the intrinsic island, as well as for the 2:1 and for higher resonances (exceptions are tiny resonances of higher order, such as the 3:2 resonance, see [21,23]). To launch nondispersive wave packets along the frozen-planet orbit of the real three-dimensional atom, an additional perturbation of the atom is therefore required, in order to stabilize the electronic motion with respect to deviations from collinearity.

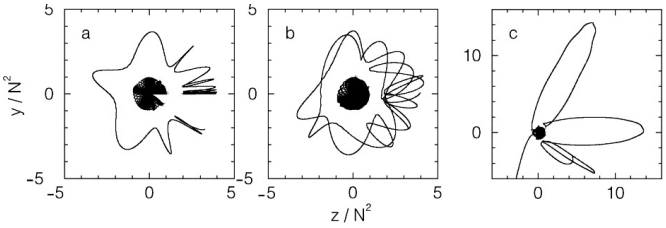

Fig. 7. Unstable trajectory of the driven frozen-planet configuration in two-dimensional configuration space. The configuration is initially launched at the center of the collinear 1:1 resonance island for $\omega = 0.25\,N^{-3}$ and $F = 0.005\,N^{-4}$ (see Fig. 5a), except for a small transverse component $y_1 = 0.01\,N^2$ of the outer electron's position. The resulting time evolution of the trajectory is depicted from 0 to 15 field cycles in (a), from 15 to 30 field cycles in (b), and from 75 to 91 field cycles in (c). We see that the initially small deviation of the configuration from the z-axis increases with time, until, after approx. 10 field cycles, both electrons flip over to the other side of the nucleus (a). The configuration then performs several chaotic rotations around the nucleus (b), before the correlation between the electrons eventually breaks down and the atom ionizes (here at about 90 field cycles) (c).

In fact, such a stabilization can be achieved by adding a *static* component $F_{\rm st}$ to the electromagnetic field (see Eq. (2)). In resonantly driven hydrogen, a static field, applied parallel to the microwave polarization axis and forcing the electron away from the nucleus, tends to confine the electron to the immediate vicinity of the polarization axis [16,22,30]. This confinement effect can now be imported to stabilize the motion of the driven frozen-planet – by preventing the configuration from chaotic rotations. Indeed, for weak static fields, $F_{\rm st} \simeq 0.1F$, and for not too strong driving amplitudes F (*e.g.*, $F = 0.005\,N^{-4}$ at $\omega = 0.25\,N^{-3}$, see Fig. 8), small deviations from collinearity do *not* lead to ionization. Instead of drifting away to the other side of the nucleus (as in the absence of the static field, Fig. 8a), the electrons are forced back towards the field polarization axis (Fig. 8b), and the configuration performs stable, quasi-periodic oscillations around the fundamental orbit shown in Figure 8c.

This stabilization mechanism permits to embed the nonlinear resonances into regular regions within the unrestricted phase space of three-dimensional motion, while the electronic dynamics within the collinear subspace is only marginally modified by the weak static field. We find that this multidimensional phase space region is

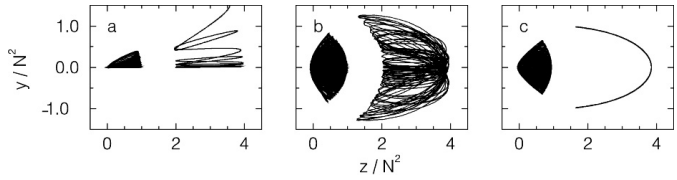

Fig. 8. Stabilization of the transverse frozen planet dynamics at $\omega = 0.25\,N^{-3}$ and $F = 0.005\,N^{-4}$. As in Figure 7, the configuration is initially launched at the center of the collinear 1:1 resonance island, except for a small transverse component $y_1 = 0.01\,N^2$ of the outer electron's position. Without the static field (a), the electrons drift away from the z-axis and enter into chaotic rotations around the nucleus. A static electric field, $F_{\rm st} = 0.1F$, along the z-axis, directed such as to force the electrons into the positive z-direction, counterbalances this drift mechanism (b); the electrons are driven back towards the z-axis, and the configuration performs stable, quasi-periodic oscillations around the fundamental orbit shown in (c).

particularly large for the 2:1 resonance (Fig. 5c): by means of the semiclassical Einstein-Brillouin-Keller (EBK) quantization criterion [31] (which typically yields rather pessimistic results, see [32]), we estimate that the minimum principal quantum number of the inner electron needed to fully localize a quantum state on the stabilized 2:1 resonance island lies in the range $N \simeq 50 \ldots 100$ [21,23]. Such double excitations are clearly beyond reach in state-of-the-art experiments on helium, which currently can excite $N \simeq 10$ [33]. However, they should be accessible in earth alkaline atoms such as barium, where multi-step isolated-core excitations [34] permit selective transitions up to states with quantum numbers $N \simeq 100$ of the inner electron [35]. At $N = 50$, the field parameters that are required to generate the 2:1 resonance islands of Figure 5c are given by $\omega/(2\pi) \simeq 20$ GHz and $F \simeq 8$ V/cm. Hence, by virtue of this semiclassical argument, nondispersive two-electron wave packets appear realizable in earth alkalines, at microwave frequencies and field amplitudes commonly used in state-of-the-art ionization experiments on one-electron atoms [36].

3 Formulation of the quantum eigenvalue problem

3.1 The collinear Hamiltonian

The preceding classical analysis strongly suggests the existence of nondispersive wave packets which propagate along the frozen-planet orbit, together with a rough estimate of the minimum required quantum number for their unambiguous identification in the spectrum of doubly excited helium. Reliable information on the quantum properties of the field-induced resonances, however, can only be obtained by quantum calculations. In particular, classical mechanics tells nothing about the lifetimes of the wave packets, since these are associated with a classically forbidden tunneling process. It is, on the other hand, also clear that a full-blown quantum treatment of such highly correlated states under external driving is still beyond reach of the presently available computational facilities. For *unperturbed* helium, where the total angular momentum is conserved, autoionizing states can presently be calculated for quantum numbers of the inner electron reaching $N \simeq 15 \ldots 20$ [19,37]. Therefore, in the near future there is not much hope for an accurate treatment of the periodically *driven* problem, with a large number of angular momenta coupled by the field, at comparable or even higher excitations.

Nevertheless, essential *qualitative* information on the wave packets can be obtained by an approximate quantum description, which is motivated by the classical motion of the electrons. As discussed in the previous section, the static field confines the electrons to the vicinity of the field polarization axis (Fig. 8), without major modifications of the dynamics in the collinear subspace. Hence, also a quantum state associated with the transversely stabilized wave packet orbit should exhibit strong localization close to the z-axis. We therefore expect that essential properties of such a quantum state are reproduced by a *collinear* model which restricts the electrons to move along the field polarization axis. This, however, requires that the model takes into account the *full* Coulomb interaction between the charged particles (*i.e.*, that it really represents the exact quantum analog of the classical, collinear configuration). A smoothing of the Coulomb singularity, which is frequently employed in one-dimensional models of driven atoms (*e.g.*, [38]), may not be permitted, since it allows the electrons to penetrate to the other side of the nucleus, what inevitably destroys the frozen-planet configuration.

Consequently, we write the Hamiltonian that generates the quantum dynamics of the driven collinear configuration as

$$H = -\frac{1}{2}\frac{\partial^2}{\partial z_1^2} - \frac{1}{2}\frac{\partial^2}{\partial z_2^2} - \frac{Z}{z_1} - \frac{Z}{z_2} + \frac{1}{z_1 - z_2} - \frac{F}{\omega}\sin\omega t\left(\frac{1}{\mathrm{i}}\frac{\partial}{\partial z_1} + \frac{1}{\mathrm{i}}\frac{\partial}{\partial z_1}\right) - F_{\rm st}\,(z_1 + z_2), \quad (4)$$

where the *exact* Coulomb interactions between the charged particles are taken into account. Here, z_1 and z_2 represent the *Cartesian* (not spherical) coordinates of the electrons along the field polarization axis, with $0 < z_2 < z_1 < \infty$ – *i.e.*, both electrons are located on the same side of the nucleus, with electron 2 closer to it than electron 1. Note that the electrons effectively appear as *distinguishable* particles. This ansatz is consistent with the restriction to collinear motion, since in the classical collinear configuration the electrons are not able to pass each other and to exchange their positions, nor do their quantum wave functions appreciably overlap at the instant of closest approach (what can be deduced from the classical dynamics sketched in Fig. 2, amended by Heisenberg's uncertainty). Furthermore, it represents quite good an approximation also for the three-dimensional frozen-planet configuration, since the latter is characterized by a very small overlap between the outer and the inner electron's densities, and therefore by a very small splitting between singlet and triplet states [19]. Precisely as for the classical

Hamiltonian, the external electric field consists of an oscillating part F – which, in contrast to (1), is incorporated in the velocity gauge in order to ensure better convergence of the numerical calculation [39] – and of a static component $F_{\rm st} > 0$ which forces the electrons away from the nucleus.

In a last step, we introduce the coordinates

$$\xi = z_1 - z_2\,, \eta = z_2\,, \tag{5}$$

which independently lie in the range $0 \leq \xi, \eta \leq \infty$. In these *perimetric coordinates* [40], the Hamiltonian is rewritten as

$$H = -\frac{\partial^2}{\partial\xi^2} - \frac{1}{2}\frac{\partial}{\partial\eta^2} + \frac{\partial^2}{\partial\xi\partial\eta} - \frac{Z}{\xi+\eta} - \frac{Z}{\eta} + \frac{1}{\xi} - \frac{F}{\omega}\sin\omega t\,\frac{1}{\rm i}\frac{\partial}{\partial\eta} - F_{\rm st}\,(\xi+2\eta), \tag{6}$$

what will turn out as a convenient form for our further treatment.

3.2 Floquet theory and complex scaling

Due to the temporal periodicity of the Hamiltonian, the Schrödinger problem represented by (6) is conveniently treated in the framework of Floquet theory [41,42]: any solution of the Schrödinger equation can be expanded in a set of $2\pi/\omega$-periodic quasienergy-eigenfunctions $\psi_t^{(\mathcal{E})}$,

$$\psi_t = \sum\!\!\!\!\!\!\int {\rm d}\mathcal{E} C_{\mathcal{E}} \psi_t^{(\mathcal{E})} {\rm e}^{-{\rm i}\mathcal{E}\,t}, \quad \text{with} \quad \psi_{t+2\pi/\omega}^{(\mathcal{E})} = \psi_t^{(\mathcal{E})}\,, C_{\mathcal{E}} \in \mathbb{C} \tag{7}$$

which satisfy the Floquet eigenvalue equation

$$\left(H - {\rm i}\,\frac{\partial}{\partial t}\right)\psi_t^{(\mathcal{E})} \;=\; \mathcal{E}\,\psi_t^{(\mathcal{E})}. \tag{8}$$

A Fourier series expansion of $\psi_t^{(\mathcal{E})}$,

$$\psi_t^{(\mathcal{E})} = \sum_{k=-\infty}^{\infty} \hat{\psi}_k^{(\mathcal{E})} {\rm e}^{{\rm i}\,k\,\omega\,t}, \tag{9}$$

yields a *time-independent* eigenvalue problem for the Fourier components $\hat{\psi}_k^{(\mathcal{E})}$, where the effective Hamiltonian matrix contains the stationary part of the Hamiltonian shifted by $k\omega$ as diagonal, and the Fourier components of the periodic driving as off-diagonal (block) elements. This results in an ω-periodic spectrum of quasienergies $\mathcal{E}$.

For atomic systems, the Floquet spectrum is absolutely continuous: each bound state of the unperturbed atom is coupled to the atomic continuum *via* multiphoton transitions, and therefore appears as a resonance structure in the spectrum – in analogy to autoionizing states in multiply excited atoms, which are coupled to the continuum *via* configuration interaction [43] (see, *e.g.*, [44] for a case in triply excited lithium). In order to separate these resonances from the flat background of the continuous spectrum, we use the method of complex scaling [45–47]. It consists in the complexification of coordinates and momenta (*not* of time!) according to[1]

$$\begin{aligned} \xi \;&\longrightarrow\; \xi{\rm e}^{{\rm i}\theta} \qquad -{\rm i}\frac{\partial}{\partial\xi} \;\longrightarrow\; -{\rm i}\frac{\partial}{\partial\xi}{\rm e}^{-{\rm i}\theta} \\ \eta \;&\longrightarrow\; \eta{\rm e}^{{\rm i}\theta} \qquad -{\rm i}\frac{\partial}{\partial\eta} \;\longrightarrow\; -{\rm i}\frac{\partial}{\partial\eta}{\rm e}^{-{\rm i}\theta}, \end{aligned} \tag{10}$$

through application of the *nonunitary* complex scaling operator $R(\theta)$ on $\psi_t^{(\mathcal{E})}$,

$$R(\theta)\psi_t^{(\mathcal{E})}(\xi,\eta) = {\rm e}^{{\rm i}\theta}\psi_t^{(\mathcal{E})}(\xi{\rm e}^{{\rm i}\theta}, \eta{\rm e}^{{\rm i}\theta}) =: \psi_{\theta,t}^{(\mathcal{E})}(\xi,\eta)\,. \tag{11}$$

Accordingly, the Hamiltonian is transformed as

$$H \;\longrightarrow\; H_\theta = R(\theta)\,H\,R(-\theta), \tag{12}$$

what turns (8) into a complex symmetric rather than hermitian eigenvalue problem, with eigenvalues in the lower half of the complex plane. In particular, resonances of the "real" eigenvalue problem (*i.e.*, at $\theta = 0$) appear, for finite θ, as isolated, *discrete* complex eigenvalues $\mathcal{E} = E - {\rm i}\Gamma/2$: their real and imaginary parts correspond to the energies E and to the half widths at half maximum $\Gamma/2$ (HWHM) of the resonances, respectively.

3.3 Expansion in Sturmian basis functions

The complex-scaled Floquet Hamiltonian is now expanded in the product basis

$$\{S_n^{(\alpha)}(\xi) S_m^{(\beta)}(\eta)\colon\, n,m \geq 1\} \tag{13}$$

composed of the real-valued Sturmian functions [48]

$$S_n^{(\alpha)}(\xi) \;=\; \frac{(-1)^n}{\sqrt{n}}\,\frac{2\xi}{\alpha}\,\exp\left(-\frac{\xi}{\alpha}\right) L_{n-1}^{(1)}\left(\frac{2\xi}{\alpha}\right), \tag{14}$$

where the $L_{n-1}^{(1)}$ denote the associated Laguerre polynomials [49]. The real parameter $\alpha > 0$ fixes the length scale of the Sturmians. As a consequence, the product basis (13) exhibits two independent scaling parameters, α and β, which permit the optimal tuning of the basis with respect to the relative excitation of the electrons. Also note that the Sturmians $S_n^{(\alpha)}$ scale at least linearly with ξ, for $\xi \to 0$. This implies that the Coulomb singularities of the Hamiltonian (6) do not lead to divergent matrix elements in the product basis (13).

Multiplication of (8) by $\xi\eta$ leaves $1/(\xi+\eta)$ as the only non-polynomial contribution in ξ and η, after inserting (6). We factor out $(\xi+\eta)$ from the eigenvectors of (8),

$$\psi_t^{(\mathcal{E})}(\xi,\eta) \;=:\; (\xi+\eta)\,\phi_t^{(\mathcal{E})}(\xi,\eta)\,, \tag{15}$$

[1] Note that, due to (5), complexification of ξ, η and of z_1, z_2 is equivalent.

and expand $\phi_t^{(\mathcal{E})}(\xi,\eta)$ in the Sturmian product basis. This factorization is justified since the triple collision between the electrons and the nucleus – *i.e.*, the event that corresponds to $\xi = \eta = 0$ – is classically suppressed in the collinear frozen-planet dynamics (in contrast to the eZe configuration with the electrons on opposite sides of the nucleus); hence, the quantum probability near $\xi = \eta = 0$ is very small. Note that, due to normalization, (15) entails a different transformation law for $\phi_t^{(\mathcal{E})}(\xi,\eta)$ as compared to $\psi_t^{(\mathcal{E})}(\xi,\eta)$, under the action of $R(\theta)$:

$$R(\theta)\phi_t^{(\mathcal{E})}(\xi,\eta) = \mathrm{e}^{2\mathrm{i}\theta}\phi_t^{(\mathcal{E})}(\xi\mathrm{e}^{\mathrm{i}\theta},\eta\mathrm{e}^{\mathrm{i}\theta}) =: \phi_{\theta,t}^{(\mathcal{E})}(\xi,\eta)\,. \quad (16)$$

All together, the generalized Floquet eigenvalue equations finally reads

$$(\xi+\eta)\xi\eta(H_{0\theta}+k\omega-\mathcal{E})(\xi+\eta)\hat{\phi}_{\theta,k}^{(\mathcal{E})}(\xi,\eta) + (\xi+\eta) \times \xi\eta V_\theta(\xi+\eta)(\hat{\phi}_{\theta,k-1}^{(\mathcal{E})}(\xi,\eta) - \hat{\phi}_{\theta,k+1}^{(\mathcal{E})}(\xi,\eta)) = 0\,, \quad (17)$$

with the complex scaled operators $H_{0\theta}$, V_θ given by

$$H_{0\theta} = \left(-\frac{\partial}{\partial\xi^2} - \frac{1}{2}\frac{\partial}{\partial\eta^2} + \frac{\partial^2}{\partial\xi\partial\eta}\right)\mathrm{e}^{-2\mathrm{i}\theta} + \left(-\frac{Z}{\xi+\eta} - \frac{Z}{\eta} + \frac{1}{\xi}\right)\mathrm{e}^{-\mathrm{i}\theta} - F_{\mathrm{st}}\,(\xi+2\eta)\,\mathrm{e}^{\mathrm{i}\theta}, \quad (18)$$

$$V_\theta = \frac{F}{2\omega}\,\frac{\partial}{\partial\eta}\,\mathrm{e}^{-\mathrm{i}\theta}, \quad (19)$$

and the $\hat{\phi}_{\theta,k}^{(\mathcal{E})}(\xi,\eta)$ the Fourier components (see (9)) of the wavefunction $\phi_{\theta,t}^{(\mathcal{E})}(\xi,\eta)$. Introducing the scalar product

$$\widetilde{\langle f\,|g\rangle} \;\equiv\; \int_0^\infty\int_0^\infty \frac{1}{\xi\,\eta}\,f(\xi,\eta)\,g(\xi,\eta)\,\mathrm{d}\xi\,\mathrm{d}\eta\,, \quad (20)$$

with respect to which the Sturmians are orthogonal, we obtain a complex symmetric eigenvalue problem.

All the opertor-valued terms acting on the $\hat{\phi}_{\theta,k}^{(\mathcal{E})}$ and $\hat{\phi}_{\theta,k\pm1}^{(\mathcal{E})}$ in (17) can now be expressed as polynomials of the elementary ladder operators of the Sturmian basis (14) (see [23,49]). Hence, upon expansion of the Fourier components $\hat{\phi}_{\theta,k}^{(\mathcal{E})}$ in the Sturmian product basis (13),

$$\hat{\phi}_{\theta,k}^{(\mathcal{E})}(\xi,\eta) \;=\; \sum_{m,n=1}^{\infty} C_{n,m}^{(k)}\,S_n^{(\alpha)}(\xi)\,S_m^{(\beta)}(\eta)\,, \quad (21)$$

we obtain strict selection rules which permit nonzero couplings between the coefficients $C_{n,m}^{(k)}$ and $C_{n',m'}^{(k')}$ only if $|n-n'|\le 4$, $|m-m'|\le 4$, and $|k-k'|\le 1$. The eigenvalue problem thus becomes a sparse, complex symmetric matrix equation with rather narrow bandwidth, what allows to apply efficient diagonalization methods based on the Lanczos algorithm with inverse iteration [50]. Convergence of the complex eigenvalues is controlled by increasing the number of Fourier components $\hat{\phi}_{\theta,k}^{(\mathcal{E})}$ and of the basis functions $S_n^{(\alpha)}(\xi)$, $S_m^{(\beta)}(\eta)$ to be retained in the diagonalization, as well as by variation of the complex scaling angle θ, and of the length scale parameters α and β which specify the (truncated) basis set (14) used in the calculation. Typical matrix dimensions are 64 000 (size) $\times$ 1 300 (bandwidth) for Floquet spectra in the vicinity of $N \simeq 8$, with $n \simeq 1\ldots150$, $m \simeq 1\ldots25$, and $k \simeq -8\ldots8$, for[2] $\omega \simeq 0.2N^{-3}$. Real and complex scaling parameters are fixed at $\theta = 0.1$, $\alpha = 6$, $\beta = 2$ in the above energy range. With these choices (and similar choices for other values of N), all numerical results presented hereafter are converged to an absolute accuracy of $10^{-15}\ldots10^{-13}$ a.u.

3.4 Visualization of the wavefunction

The energies E and widths Γ extracted from the complex eigenvalues $\mathcal{E}$ allow to classify the Floquet states in series and to determine their stability; in general, however, they do not provide any direct information about the localization properties of these states in configuration or in phase space, which in themselves can carry important physical information. To extract the latter from the eigenstates of the complex symmetric eigenvalue problem (17), some care has to be taken, due to the non-unitarity of the dilation operator $R(\theta)$. The technical and computational details of this procedure are described in detail in [23,51], and we only import here those results of immediate relevance for our specific purpose.

We first need the density of the physical wave function (at *real* energy E) $\psi_t^{(\mathcal{E})}(z_1,z_2)$, which is obtained (up to a normalization constant), for a well-isolated resonance energy $\mathcal{E} = E - \mathrm{i}\Gamma/2$ (*i.e.*, $|\mathcal{E}_j - \mathcal{E}| \gg \Gamma\,, \forall\mathcal{E}_j \neq \mathcal{E}$), from the image of $\psi_{\theta,t}^{(\mathcal{E})}$ under the inverse dilation operator $R(-\theta)$,

$$R(-\theta)\psi_{\theta,t}^{(\mathcal{E})} = R(-\theta)\sum_{k=-\infty}^{\infty} z_1\hat{\phi}_{\theta,k}^{(\mathcal{E})}\,(z_1-z_2,z_2)\,\mathrm{e}^{\mathrm{i}k\omega t}\,, \quad (22)$$

together with the image of the corresponding left eigenvector $\psi_{\theta,-t}^{(\mathcal{E})}$ [23,51][3]:

$$|\psi_t^{(\mathcal{E})}(z_1,z_2)|^2 \simeq \mathrm{Re}\langle z_1,z_2|R(-\theta)|\psi_{\theta,t}^{(\mathcal{E})}\rangle \times \left\langle z_1,z_2|R(-\theta)|\psi_{\theta,-t}^{(\mathcal{E})}\right\rangle. \quad (23)$$

Correspondingly, the Husimi representation $Q(z_1,p_1)$ [23,51] in the classical phase space coordinates of the *outer* electron (subscript 1) is obtained by projection on Gaussian

[2] Note that a nonvanishing static field component does only increase the bandwidth of the Floquet matrix ($|n-n'|\le 4$ instead of $|n-n'|\le 3$ [23]) but not its dimension, which is a peculiarity of the absence of the angular momentum degree of freedom in our collinear model.

[3] Only the time-dependent part of the wave function is complex conjugated to transform right into left eigenvectors, since the Fourier components $\hat{\psi}_{\theta,k}^{(\mathcal{E})}$ of the eigenvectors obey the normalization condition for complex symmetric rather than Hermitian matrices [6,23]!

wave packets $\chi_{p_1}(z_1)$ which are centered at position z_1 and propagate with average momentum p_1:

$$Q(z_1,p_1) \simeq \mathrm{Re}\left\langle \chi_{p_1}(z_1)|R(-\theta)|\psi^{(\mathcal{E})}_{\theta,t}\right\rangle \times \left\langle \overline{\chi_{p_1}(z_1)}|R(-\theta)|\psi^{(\mathcal{E})}_{\theta,-t}\right\rangle , \quad (24)$$

where the bar denotes complex conjugation.

In order to establish a precise analogy with our above construction of the two-step Poincaré section of the classical dynamics (see Sect. 2.2), we define the overlap matrix element in (24) as

$$\langle \chi_{p_1}(z_1)|R(-\theta)|\psi^{(\mathcal{E})}_{\theta,t}\rangle = \int_0^\infty \mathrm{d}z_1' \, \langle z_1', z_2^{(0)}|R(-\theta)|\psi^{(\mathcal{E})}_{\theta,t}\rangle \times \exp\left(-\frac{1}{2}\omega_s(z_1-z_1')^2 - \mathrm{i}p_1 z_1'\right) . \quad (25)$$

Thus, the quantum phase space probability density is evaluated at fixed time t (corresponding to a fixed phase ωt of the driving field), and at fixed position $z_2^{(0)} \simeq 0$ of the inner electron. The *squeezing parameter* ω_s in this definition determines the resolution of the Husimi distribution in position and momentum, respectively. Large values of ω_s yield good resolution in position space and bad resolution in momentum space, and *vice versa* for small values of ω_s. For quantum states associated with the frozen-planet configuration, the most appropriate choice for ω_s is given by the intrinsic frequency scale ω_I of the configuration (see Sect. 2.1) – this is the value at which the Gaussian wave packet $\chi_p(q)$ optimally fits the ground state of the effective potential experienced by the outer electron. We therefore choose $\omega_s = 0.3\,N^{-3}$ (see Fig. 3), with N the inner electron's principal quantum number of the state to be visualized (note that N remains approximately a good quantum number in the presence of the external field, if the latter is not too strong).

4 The unperturbed collinear atom

With the above theoretical machinery for our quantum treatment of the driven, collinear frozen planet configuration at hand, we can now study in detail its physical properties. As a "warm-up", and equally so as a first assessment of the physical implications of the restricted dimensionality of our problem, we start out with the spectral properties of the *unperturbed* ($F = F_{\mathrm{st}} = 0$) frozen planet configuration confined to a single dimension of configuration space.

4.1 Energies and phase space distributions

Corresponding to the fact that its classical counterpart is almost completely integrable (Fig. 4a), the quantum spectrum of the unperturbed collinear frozen-planet configuration is characterized by typical signatures of regular

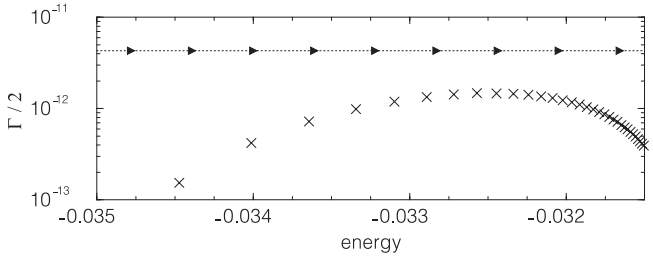

Fig. 9. Energies and ionization rates $\Gamma/2$ (HWHM) of the autoionizing states of collinear helium belonging to the series labeled by the inner electron's quantum number $N = 8$. Note the relatively small widths of the lowest members of the series, which we attribute to the fact that these states are fully localized within a regular, bound domain in phase space. The coupling mediated by a driving field with frequency $\omega = 0.2\,N^{-3}$ is sketched by the arrows of length ω. The particularly strong, near-resonant coupling between the second and the third state (at $E = -0.034$ and $E = -0.0336$, respectively) gives rise to the nondispersive two-electron wave packet associated with the classical 1:1 resonance (see Fig. 13).

dynamics. In particular, each autoionizing state can be classified by two quantum numbers which are associated with the two separating modes of the classical dynamics, as discussed in Section 2.1 (in contrast to the chaotic eZe configuration [52], where such a classification breaks down already for moderate double excitations). The quantization of the inner electron's Kepler mode gives rise to the quantum number $N \geq 1$. For each N, we obtain a series of autoionizing states (or bound states, for $N = 1$) which are labeled by the quantum number n. This quantum number arises from the quantization of the outer electron's oscillation within the effective potential, which, as in one-electron atoms, gives rise to Rydberg series and continua, due to its asymptotic $1/r$ dependence.

As an example, we show the energies and widths of the autoionizing states of the series labeled by $N = 8$ in Figure 9. We clearly recognize a regular Rydberg progression towards the $N = 8$ threshold at $E = -0.3125$ a.u. States belonging to different series are energetically well separated: the lowest quantum state with $N = 9$ lies at $E \simeq -0.027$ a.u., and the Rydberg series of $N = 7$ terminates at $E \simeq -0.04$ a.u. As was verified numerically, an energetic overlap of series belonging to different quantum numbers N occurs only above $N = 20$.

The near-separability of the two modes associated with the electrons is furthermore reflected by the probability density (23) of the eigenstates (with $k = 0$ in (22), due to the time-independence of the problem). In the coordinate z_2 of the inner electron, the wavefunctions are essentially given by the Nth hydrogenic eigenstate of the one-dimensional atom (most reminiscent of extremal parabolic states of three-dimensional atomic hydrogen), whereas in z_1 they display distinct excitations within the effective potential governing the outer electron's motion. In Figure 10, the fundamental (a1), the first excited (a2), and the second excited state (a3) of the effective potential (for $N = 8$), labeled by the outer electron's quantum

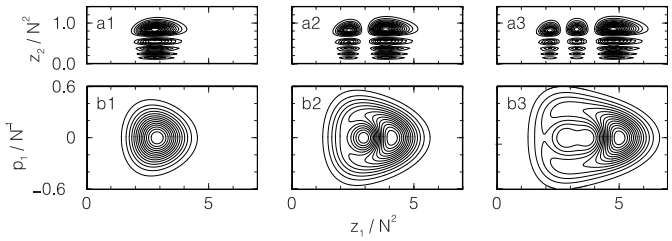

Fig. 10. Wavefunctions of the first three eigenstates of the $N = 8$ series: (a1, b1) lowest ($n = 1$), (a2, b2) second ($n = 2$), (a3, b3) third state ($n = 3$) of the series. (a1–a3) Probability densities as a function of the coordinates of the outer (z_1) and of the inner (z_2) electron; (b1–b3) Husimi densities as a function of position and momentum of the outer electron (the contour lines are plotted on a linear scale). In the coordinate of the inner electron, the wavefunctions are essentially given by the Nth hydrogenic eigenstate of the unperturbed, one-dimensional atom, whereas in z_1 they display different excitations within the effective potential (see Fig. 3). Their Husimi distributions clearly show that they are well localized along regular tori in the underlying classical phase space (see Fig. 4a).

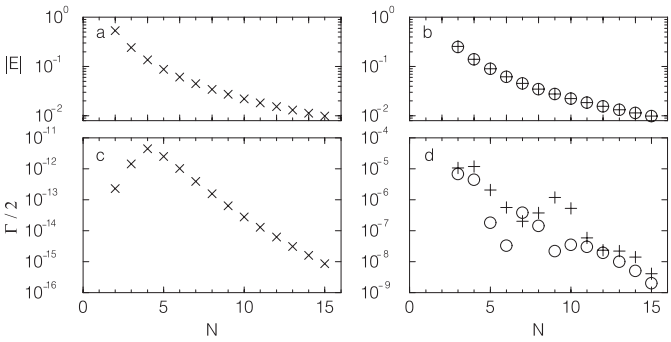

Fig. 11. Energies (a) and ionization widths (c) of the lowest autoionizing eigenstate $n = 1$ (with the outer electron localized at the minimum of the effective potential of Fig. 3), plotted as a function of the inner electron's quantum number N. We see that the ionization rates decrease near-exponentially for $N > 4$, what suggests that the associated eigenstates are fully localized in the bound part of phase space, and only decay *via* tunneling through the classical phase space barriers that protect the frozen-planet configuration against classical autoionization. These rates of the collinear model are compared to the energies (b) and decay rates (d) of the analogous frozen-planet eigenstates in three-dimensional helium, published in reference [19], for singlet (+) and triplet (∘) symmetry. While the energies agree quite well with their collinear counterparts (a, b), the ionization rates of the three-dimensional frozen-planet states (d) lie by several orders of magnitude above the widths of the corresponding eigenstates of the one-dimensional model (c) (note the different scales of the vertical axes in (c) and (d)). This indicates that the autoionization of the three-dimensional frozen-planet states is mediated by the transverse degrees of freedom of the configuration.

numbers $n = 1$, $n = 2$, and $n = 3$, respectively, are plotted in configuration space. The intimate correspondence of these eigenstates with regular structures of the underlying classical phase space is highlighted by their Husimi distribution (24) shown in Figures 10b1–10b3. Comparing these phase space projections of the quantum eigenfunctions with the corresponding Poincaré surface of section (Fig. 4a) unambiguously illustrates the neat localization of the eigenfunctions along invariant tori of the classical dynamics.

4.2 Ionization rates

The "regular" character of the wavefunctions is also manifest in the ionization rates $\Gamma/2$ (HWHM) of the associated spectral resonances. We see in Figure 9 that for the $N = 8$ series these widths first increase with n, and then decrease again towards the ionization threshold. While this latter decrease is attributed to general scaling laws of Γ in the Rydberg regime of atomic one-electron excitations [53], the extraordinary stability of low n states is a consequence of their full localization in the bound part of phase space. A coupling to the unbound, ionizing domain is then only possible *via* a classically forbidden process – tunneling through the phase space barriers that confine the frozen-planet configuration.

This latter mechanism is beautifully illustrated in a plot of the ionization rate of the lowest state ($n = 1$) as a function of the inner electron's quantum number N. In Figure 11c, we observe that the width of this lowest eigenstate in the effective potential of Figure 3 first increases for $N \leq 4$ (due to imperfect localization of the eigenstate on classical phase space structures in the deep quantum regime) and then decreases exponentially with N. This exponential law represents a clear signature of quantum tunneling: the rate associated with such a process generally decreases exponentially with the semiclassical action S_N across the tunneling barrier, and this latter quantity scales, as any other action variable, linearly with N, due to the general scaling laws (3) – *i.e.*, $S_N = NS_1$, with $S_1 \simeq 0.8$ directly extracted from Figure 11c.

For comparison, we plot in Figure 11d the ionization rates of the near-collinear frozen-planet states in three-dimensional helium (with minimal excitations in the transverse degrees of freedom), as reported in [19]. Also these widths decrease on average exponentially in N, with a scaled action S_1 not too different from our one-dimensional model (fluctuations with respect to this exponential decrease arise from the mixed regular-chaotic phase space structure of three-dimensional helium, see also the discussion in Sect. 5.2). However, the three-dimensional rates are systematically enhanced by several orders of magnitude as compared to the one-dimensional model! This suggests that the three-dimensional helium dynamics provides efficient decay channels associated with the *transverse* degrees of freedom, which are not

incorporated in the restricted one-dimensional dynamics of our model Hamiltonian (4)[4].

On the other hand, the *energies* of the autoionizing states of three-dimensional helium agree quite well with their collinear counterparts, as apparent from Figures 11a and 11b (apart from a small shift due to the additional quantization of the transverse modes in the 3D configuration [19]). This supports our expectation that essential localization properties of the eigenstates of the three-dimensional frozen-planet configuration are well reproduced by the collinear model.

5 The collinear atom under periodic driving

5.1 Nondispersive wave packets in the Floquet spectrum

For our investigation of the collinear frozen planet configuration under external driving, we employ the field parameters $\omega = 0.2\,N^{-3}$ and $F = 0.005\,N^{-4}$ which induce the classical phase space structure shown in Figure 6, where both the intrinsic island and the 1:1 resonance are very well pronounced. The coupling induced by this driving field is illustrated by the arrows in Figure 9 for the $N = 8$ series. We see that a particularly strong interaction is induced between the second ($n = 2$) and the third ($n = 3$) state, since the energetic spacing between these states is very close to the driving frequency. Provided the phase space volume of the 1:1 resonance island is large enough to support a fully localized quantum state (which is indeed the case for $N = 8$, as can be semiclassically estimated by the EBK quantization criterion), this near-resonant one-photon coupling gives rise to the nondispersive wave packet associated with the classical nonlinear resonance.

Figure 12a shows the evolution of the quasienergies associated with the first three Floquet eigenstates of the $N = 8$ series, as a function of the field amplitude F (for fixed driving frequency $\omega = 0.2\,N^{-3}$, and $F_{\rm st} = 0$). In the limit $F = 0$, the energies E correspond to the unperturbed autoionizing levels folded into the Floquet zone due to the ω-periodicity of the Floquet spectrum. Switching on the driving field causes level shifts due to the repulsion between strongly coupled, near-resonant Floquet states. A particularly significant case is encountered for the state $n = 2$, near-resonantly coupled to the states $n = 3$ and

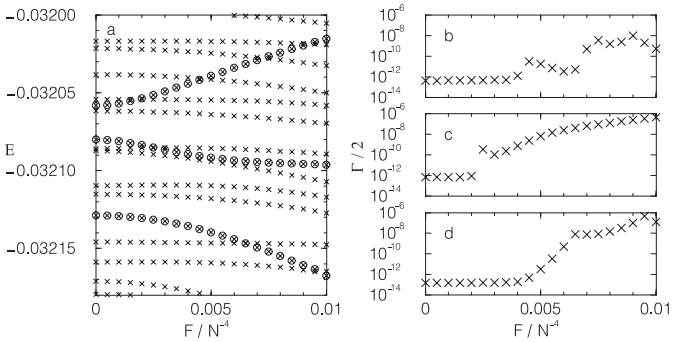

Fig. 12. (a) Evolution of the first three states of the $N = 8$ series in the Floquet spectrum, for driving frequency $\omega = 0.2\,N^{-3}$. The quasienergies E are plotted as a function of the field amplitude F. The diabatic continuation of the second state ($n = 2$, upmost circles) undergoes a particularly pronounced, almost linear shift with F. This is consistent with the wave packet character of the Floquet state into which the unperturbed $n = 2$ state evolves (see Fig. 13). (b–d) Ionization rates Γ of the diabatic continuations of the $n = 1$ (d), $n = 2$ (b), and $n = 3$ state (c). We see that the rates globally increase with increasing F. Local, pronounced maxima occur at avoided crossings between these states and energetically higher-lying eigenstates of the $N = 8$ series in the Floquet spectrum, as apparent from a comparison with (a) (with the diabatic continuations of $n = 1$ and $n = 3$ marked by the encircled eigenvalues in the lower and the middle part of (a), respectively).

$n = 1$[5]. Its quasienergy exhibits a pronounced shift at almost constant, positive slope. This already indicates the wave-packet character of the associated eigenfunction in configuration space, since it reflects a large dynamic dipole moment of the electronic density (proportional to the expectation value of the electronic dipole z_1, averaged over one cycle of the drive).

The wave packet character of this latter state is ultimately confirmed by its Husimi density, which is plotted in Figures 13b1–13b3 for $F = 0.005\,N^{-4}$, at driving phases $\omega t = 0$, $\pi/2$, and π. We see that the Floquet eigenfunction is fully localized on the 1:1 resonance island in phase space, and that it precisely follows the classical time evolution. The wave packet dynamics in configuration space is visualized in Figures 13a1–13a3 where we plot the probability density of the state $n = 2$ as a function of z_1 and z_2. Comparison with Figures 10a1–10a3 show that the eigenfunction is essentially composed of a time-periodic superposition of the low-lying eigenstates of the $N = 8$ series. While nearly stationary in the coordinate z_2 of the inner electron, the wave packet oscillates back and forth in z_1, between the turning points of the effective potential (Fig. 3).

[4] As a side remark, this observation also bears a *caveat* as oversimplified models of the three body Coulomb problem are concerned: often the Coulomb singularities in such 1D model systems are smoothed such as to prevent the electrons (and possibly the nucleus) from head-on collisions [54,55], which, on a first glance, could be most disastrous for the stability of the 1D dynamics and, hence, *enhance* its decay probability. The present comparison of exact (no approximations beyond dimensionality) 1D and 3D quantum calculations shows that this is too simplistic an argument and completely neglects dynamical stabilization effects which result in such impressively stable quantum objects as the frozen planet.

[5] Note that the field induced level dynamics which we observe here is somewhat reminiscent to the level shift of the lowest three energy levels of a symmetric one dimensional double well, under resonant driving of the transition between the first and second excited state [56]. A more general investigation of Floquet level dynamics in complex, non-decaying systems can be found, *e.g.*, in [57].

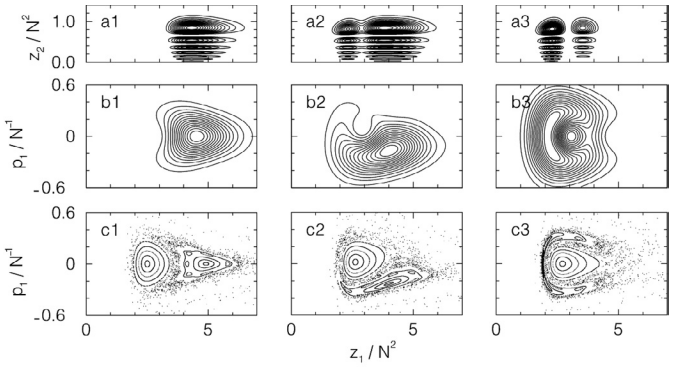

Fig. 13. Nondispersive two-electron wave packet of the $N = 8$ series, for $\omega = 0.2\,N^{-3}$ and $F = 0.005\,N^{-4}$. We plot the probability density in configuration space (a1–a3), and the Husimi density in phase space (b1–b3), of the diabatic continuation of the state $n = 2$ (see Fig. 12), at driving field phases (a1–c1) $\omega t = 0$, (a2–c2) $\pi/2$, (a3–c3) π. The corresponding Poincaré sections of the classical phase space are plotted in (c1–c3). We see that the Floquet wavefunction is well localized on the 1:1 resonance island, and faithfully tracks its classical time evolution.

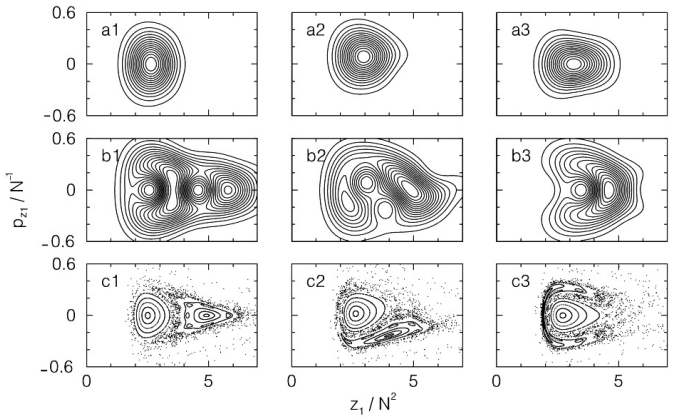

Fig. 14. Husimi distribution of the states $n = 1$ (a1–a3) and $n = 3$ (b1–b3) of the $N = 8$ series, for $\omega = 0.2\,N^{-3}$ and $F = 0.005\,N^{-4}$, at driving phases $\omega t = 0$ (a1, b1), $\pi/2$ (a2, c2), π (a3, b3), compared to the corresponding classical Poincaré sections (c1–c3). We see that the diabatic continuation of the lowest state of the $N = 8$ series is fully localized on the intrinsic island and remains essentially stationary over one field cycle. The diabatic continuation of the third state, on the other hand, is associated with the chaotic phase space domain. More precisely, it is anchored to the unstable fixed point of the 1:1 resonance and stretches out along the associated separatrix structure (see also [8,16] for analogous states in driven hydrogen atoms).

Quite naturally, for the same field amplitude and frequency as above, the diabatic continuation of the lowest state $n = 1$ of the $N = 8$ series represents the Floquet state that is anchored to the remainder of the unperturbed regular structure of the frozen-planet configuration. Figures 14a1–14a3 show its Husimi distribution which is fully localized on the intrinsic island and remains nearly stationary over one field period. Furthermore, Floquet states corresponding to higher quantum numbers $n > 2$ of the unperturbed system are entirely associated with the chaotic phase space domain. As an example, Figures 14b1–14b3 show the Husimi density of the diabatic continuation of the state $n = 3$, which is dominantly localized on the unstable fixed point of the 1:1 resonance (compare Figs. 14b3 and 14c3), and along the associated separatrix layer.

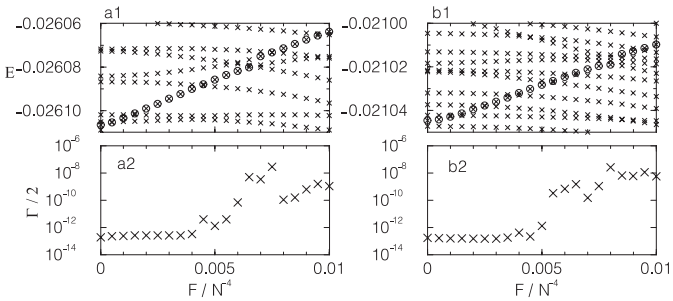

Fig. 15. Energies and widths of the nondispersive wave packet at $\omega = 0.2\,N^{-3}$ for $N = 9$ (a1, a2) and $N = 10$ (b1, b2), as a function of the scaled field amplitude F/N^{-4}. (a1, b1) Evolution of the quasienergies E in the Floquet spectrum. The 1:1 resonance state (marked by circles) diabatically originates from the unperturbed state $n = 2$ at $N = 9$, and from the state $n = 3$ at $N = 10$. As for $N = 8$ (see Fig. 12a), its quasienergy undergoes a significant shift towards higher values of E with almost constant slope, what indicates the pronounced wave packet character of this eigenstate in configuration space. (a2, b2) Ionization widths of the wave packet states. As in Figure 12c, local, sharp enhancements of Γ occur near avoided crossings with higher-lying states of the same series, which are associated with the chaotic phase space domain. Notice that the precise positions and strengths of the avoided crossings and, consequently, their influence on the wave packet's lifetime at a given scaled field amplitude F/N^{-4}, can be completely different for N (a1, a2) and $N + 1$ (b1, b2).

A similar scenario is encountered for different quantum numbers N of the inner electron (with adjusted field parameters $\omega = 0.2\,N^{-3}$ and $F = 0.005\,N^{-4}$). Starting from $N = 5$, we find, for each N, one Floquet state that is localized on the intrinsic island (the diabatic continuation of the island's ground state in the unperturbed spectrum), as well as one nondispersive wave packet state localized on the 1:1 resonance island, represented by the diabatic continuation of the second unperturbed state for $N < 10$, and by the continuation of the third or a higher state for $N \geq 10$. As for $N = 8$, these wave packet states are characterized by a pronounced, almost linear level shift with increasing F towards higher quasienergies (Fig. 15).

Figure 16 compares the Husimi distributions of the wave packet states for $N = 5$ and $N = 15$. Since the phase space area of the island increases linearly with N while $\hbar$ remains constant, the electronic density is, with increasing N, more and more localized around the center of the 1:1 resonance island. At $N = 15$, the contour lines of the Husimi density reproduce the classical island structure in the Poincaré section already very well. In fact, at such high values of N, the island is already large enough

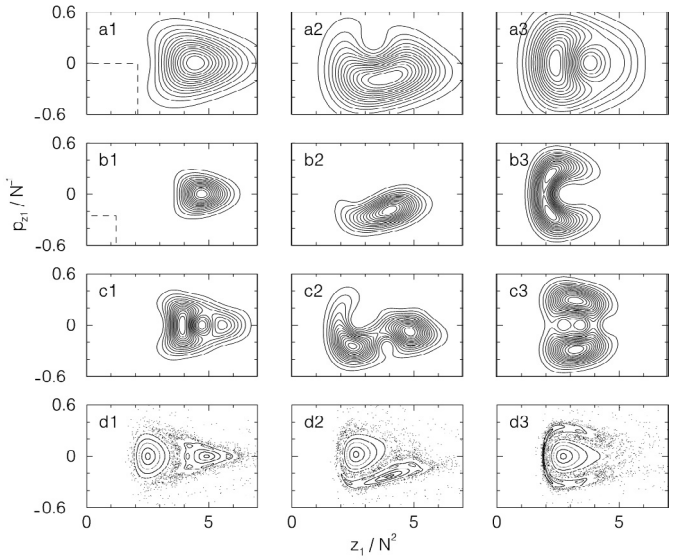

Fig. 16. Nondispersive two-electron wave packet for $N = 5$ (a1–a3) and $N = 15$ (b1–b3), as well as the first excited mode of the nondispersive wave packet for $N = 15$ (c1–c3), at $\omega = 0.2\,N^{-3}$ and $F = 0.005\,N^{-4}$. The Husimi density of the Floquet states is plotted for the phases (a1–d1) $\omega t = 0$, (a2–d2) $\pi/2$, (a3–d3) π, and compared to the corresponding classical Poincaré sections (d1–d3). With increasing N, the wave packet is more and more localized on the center of the 1:1 resonance, due to the decreasing relative size of $2\pi\hbar$ (as compared to the typical atomic scales, see Eqs. (3)) indicated by the dashed rectangles in (a1) and (b1). At $N = 15$, the contour lines of the Husimi density reproduce the structure of the island in the classical Poincaré section rather well.

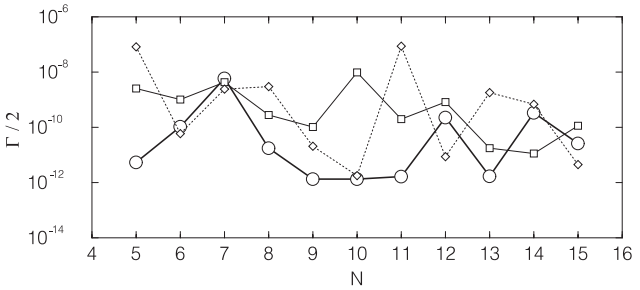

Fig. 17. Ionization rates (HWHM) of the wave packet state localized on the 1:1 resonance island, as a function of the inner electron's quantum number N ($\omega = 0.2\,N^{-3}$ and $F = 0.005\,N^{-4}$), for different strengths $F_{\rm st}$ of the static field. Circles connected by thick solid lines: $F_{\rm st} = 0$; squares connected by thin solid lines: $F_{\rm st} = 0.001\,N^{-4}$; diamonds connected by dotted lines: $F_{\rm st} = 0.002\,N^{-4}$. The strong fluctuations of the rates are attributed to the coupling to Floquet states that are associated with the chaotic domain of phase space.

to trap an additional wave packet state, giving rise to a first excited mode of the nondispersive wave packet (see Figs. 16c1–16c3, and reference [10] for an analogous case in driven hydrogen).

5.2 Lifetimes of the wave packet states

As already mentioned in the introduction, the time scale over which the nondispersive wave packet follows the resonantly driven classical orbit without spreading is only limited by the finite ionization rate of the corresponding Floquet state. Since this ionization proceeds *via* a classically forbidden tunneling process, the associated decay rate is, as in driven hydrogen [6,8,10], very small. For the wave packet state of the $N = 8$ series ($\omega = 0.2\,N^{-3}$ and $F = 0.005\,N^{-4}$) for instance, we obtain $\Gamma/2 \simeq 1.77 \times 10^{-11}$ a.u., which corresponds to a lifetime of $\tau \simeq 1.8 \times 10^6$ field cycles before the wave packet population is appreciably redistributed over the ionization continuum.

In general, one expects the ionization rate of the wave packets to decrease on average exponentially $\sim \exp(-SN)$ with N, where S is the semiclassical action across the tunneling barrier that confines the resonance island at $N = 1$. In contrast to the unperturbed collinear configuration discussed in Section 4 (Fig. 11c), however, such an exponential decrease is *not* observed in our calculations. As we see in Figure 17, the ionization rates exhibit, in the range $N = 5 \ldots 15$, strong, quasi-erratic fluctuations between $\Gamma/2 \sim 10^{-12}$ a.u. and $\Gamma/2 \sim 10^{-8}$ a.u., corresponding to lifetimes between 10^4 and 10^7 field cycles. No significant tendency towards lower values for increasing N can be unambiguously identified.

The observed fluctuations of Γ represent a clear signature of the mixed regular-chaotic structure of the classical phase space (see, *e.g.*, Figs. 16d1–16d3). In contrast to globally regular systems such as the unperturbed *Zee* configuration (see Sect. 4.2), the coupling from the locally bound domain to the ionization continuum is *not* given by a single tunneling rate. Instead, it is mediated by a *two-step* process which, besides tunneling through the barriers of the regular island, involves also chaotic transport through irregular phase space outside the island towards the continuum. It is in fact this latter, chaotic component of the coupling process that generates the fluctuations of the decay rates, on top of their on average exponential decrease with N. This *chaos-assisted* tunneling mechanism, originally formulated for tunneling transitions between symmetric regular islands in bounded systems [58], was indeed proven to govern the decay of nondispersive wave packets in driven one-electron atoms [12], the latter exhibiting similar quasi-erratic deviations of Γ from a purely exponential law (see also [59]).

In the Floquet spectrum, the chaos-induced modification of the tunneling process can essentially be understood *via* the influence of near-resonant chaotic states on the ionization rate of the wave packet state. As we see in Figures 12b–12d, the widths of the energetically low-lying members of the $N = 8$ series generally increase with increasing F. Local, pronounced enhancements of Γ, however, occur near avoided crossings (corresponding to multiphoton resonances) with higher-lying states of the same series, which are associated with the chaotic phase space domain (compare Figs. 12b–12d with Fig. 12a). Hence, at a given scaled field amplitude, *e.g.* $F = 0.005N^{-4}$,

the decay rate of the wave packet state depends sensitively on the effective interaction with nearby chaotic states in the spectrum, the latter being essentially determined by the energetic distance to those states, as well as by the corresponding coupling matrix elements. Since these ingredients vary in a random-like way with the quantum number N of the inner electron (at fixed F/N^{-4}), the resulting effect on the wave packet's ionization rate may turn completely different when changing N to $N+1$ (compare here Figs. 12a, 12b to Figs. 15a1, 15a2 and 15b1, 15b2), and therefore cannot be predicted by simple semiclassical considerations.

The average exponential decrease of the ionization rate, on the other hand, should in principle be amenable to semiclassical estimations, as it is essentially determined by the height of the tunneling barrier that confines the resonance island in phase space. Semiclassical approaches to quantitatively evaluate the associated tunneling rates for nonintegrable systems are presently under construction (see [60])[6].

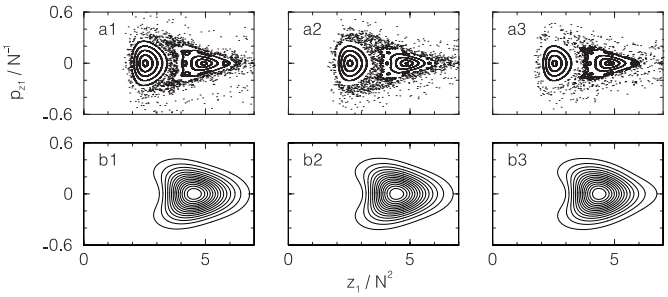

Fig. 18. (a1–a3) Poincaré section of the classical dynamics at $\omega = 0.2$ and $F = 0.005$, with a static field $F_{\rm st} = 0$ (a1), 0.001 (a2), 0.002 (a3). (b1–b3) Husimi density of the wave packet state localized on the 1:1 resonance island for $N = 8$, at $\omega = 0.2\,N^{-3}$ and $F = 0.005\,N^{-4}$, calculated in presence of a static field $F_{\rm st} = 0$ (b1), $0.001\,N^{-4}$ (b2), $0.002\,N^{-4}$ (b3) (at driving phase $\omega t = 0$). The phase space projection of the wave packet remains almost invariant when increasing the static field from $F_{\rm st} = 0$ to $0.002\,N^{-4}$, in agreement with the observation that also the classical 1:1 resonance island is largely unaffected by the additional perturbation.

5.3 Influence of an additional, static electric field

Let us finally discuss to which extent the wave packet dynamics of the collinear atom is modified by the application of an additional, static electric field with a strength of up to 20 percent of the driving field amplitude. As already pointed out in Section 2.3, such a static field is required to stabilize the driving-induced nonlinear resonances in the classical dynamics of the three-dimensional atom. While the transverse dynamics of the driven configuration is therefore substantially modified by the static field, the structure of the collinear phase space remains nearly unaffected. This is seen in Figures 18a1–18a3 which show Poincaré sections of the collinear phase space at $\omega = 0.2$ and $F = 0.005$, for gradually increasing static field components $F_{\rm st} = 0 \ldots 0.002$. Except for a slight reduction of their size, the two dominant regular islands are not significantly affected by the static perturbation.

Accordingly, we find that the phase space projections of the Floquet states localized on these islands remain essentially unmodified, too, in presence of the static field. This is illustrated in Figures 18b1–18b3 which show the resulting Husimi density of the nondispersive wave packet state of the $N = 8$ series at $\omega = 0.2\,N^{-3}$ and $F = 0.005\,N^{-4}$. However, while no visible change occurs in the phase space localization properties, the ionization rate is significantly affected by the static field: it increases from $\Gamma/2 \simeq 1.77 \times 10^{-11}$ a.u. at $F_{\rm st} = 0$, to $\Gamma/2 \simeq 3.05 \times 10^{-9}$ a.u. at $F_{\rm st} = 0.002\,N^{-4}$, corresponding to a decrease of the wave packet's lifetime from 1.8×10^6 to 1.0×10^4 field cycles. Since the static field notably affects the asymptotic part of the effective potential experienced by the outer electron (see Fig. 3), and thereby modifies the transport towards the continuum, such an enhancement of Γ with $F_{\rm st}$ is not unexpected. However, Figure 17 shows that the ionization rates do not always increase with increasing $F_{\rm st}$. Instead, a rather erratic dependence of Γ on $F_{\rm st}$ and N is encountered, what calls for a more quantitative (and possibly statistical) analysis of the problem.

6 Conclusion

Our present study provides abundant evidence for the stabilizing effect of classical nonlinear resonances on periodically driven quantum systems, in the presence of strong electron-electron interactions. We have seen that such nonlinear resonances, which actually reflect a phase locking phenomenon [16] between the unperturbed quantum dynamics and the driving field, allow to launch nondispersive two-electron wave packets along the highly correlated frozen planet orbit of collinear helium, with tiny, tunneling induced leakage towards the atomic continuum. As already observed in simpler one electron systems under external driving, these wave packets can be identified by the characteristic parameter dependence of their energies and decay rates, with strong signatures of chaos assisted ionization. Our 1D quantum calculations corroborate an intimate quantum-classical correspondence, already at rather weak excitations ($N \geq 5$) of the inner electron, even in the presence of a static electric field component added to the periodic drive (which confines the real 3D dynamics to the vicinity of the field polarization axis, in classical 3D calculations). This strongly suggests that nondispersive two-electron wave packets exist also in driven 3D helium (for which, so far, only classical

[6] Also note, that the critical field amplitude needed to induce an appreciable increase of the decay rates beyond their minimum value at small field amplitudes coincides remarkably well for $N = 8, 9, 10$, as equally observable in Figures 12 and 15. This is a signature of the transition from globally regular to dominantly chaotic dynamics in the classical phase space, and highlights the relevance of the classical scaling laws (3), also for the quantum mechanical ionization process.

simulations are feasible), and that similar stabilization phenomena are possible also in other, high dimensional atomic or molecular systems under external forcing. However, our comparison of the life times of 1D and 3D collinear frozen planet states in the absence of any external perturbation also suggest that the life times of nondispersive wave packets dramatically depend on the accessible phase space dimensions, as a direct consequence of the interelectronic repulsion – absent in single electron Rydberg dynamics. It remains to be seen whether opening one single transverse degree of freedom – by extending configuration space from the z-axis to the plane, in a 2D model (now within reach for most advanced supercomputing facilities) – suffices to restablish the order of magnitude of the (field free) 3D decay rates, and whether the confinement by the static field has a systematic effect on the rates in 2D or 3D (with or without an external drive).

It is a pleasure to acknowledge fruitful and inspiring discussions with Dominique Delande, Benoît Grémaud, Laurent Hilico, Andreas Krug, and Javier Madroñero, as well as financial support by the DAAD through the PROCOPE program.

References

1. T.C. Weinacht, J. Ahn, P.H. Bucksbaum, Nature **397**, 233 (1999)
2. X. Chen, J.A. Yeazell, Phys. Rev. Lett. **81**, 5772 (1998)
3. E. Schrödinger, Naturwissenschaften **14**, 664 (1926)
4. B. Kohler *et al.*, Phys. Rev. Lett. **74**, 3360 (1995)
5. I.S. Averbukh, M.J.J. Vrakking, D.M. Villeneuve, A. Stolow, Phys. Rev. Lett. **77**, 3518 (1996)
6. A. Buchleitner, Ph.D. thesis, Université Pierre et Marie Curie, Paris, 1993
7. D. Delande, A. Buchleitner, Adv. At. Mol. Opt. Phys. **35**, 85 (1994)
8. A. Buchleitner, D. Delande, Phys. Rev. Lett. **75**, 1487 (1995)
9. I. Bialynicki-Birula, M. Kaliński, J.H. Eberly, Phys. Rev. Lett. **73**, 1777 (1994)
10. J. Zakrzewski, D. Delande, A. Buchleitner, Phys. Rev. Lett. **75**, 4015 (1995)
11. K. Sacha, J. Zakrzewski, Phys. Rev. A **59**, 1707 (1999)
12. J. Zakrzewski, D. Delande, A. Buchleitner, Phys. Rev. E **57**, 1458 (1998)
13. B.E. Sauer, M.R.W. Bellermann, P.M. Koch, Phys. Rev. Lett. **68**, 1633 (1992)
14. G.P. Berman, G.M. Zaslavsky, Phys. Lett. **61A**, 295 (1977)
15. J. Henkel, M. Holthaus, Phys. Rev. A **45**, 1978 (1992)
16. A. Buchleitner, D. Delande, J. Zakrzewski, Phys. Rep. **368**, 409 (2002)
17. K. Richter, G. Tanner, D. Wintgen, Phys. Rev. A **48**, 4182 (1993); D. Wintgen, K. Richter, G. Tanner, Chaos **2**, 19 (1992)
18. K. Richter, D. Wintgen, Phys. Rev. Lett. **65**, 1965 (1990)
19. K. Richter, J.S. Briggs, D. Wintgen, E.A. Solov'ev, J. Phys. B **25**, 3929 (1992)
20. P. Schlagheck, A. Buchleitner, J. Phys. B **31**, L489 (1998)
21. P. Schlagheck, A. Buchleitner, Physica D **131**, 110 (1999)
22. J.G. Leopold, D. Richards, J. Phys. B **20**, 2369 (1987)
23. P. Schlagheck, *Das Drei-Körper-Coulombproblem unter periodischem Antrieb*, Ph.D. thesis, Technische Universität München, Herbert Utz Verlag, München, 1999
24. P. Schlagheck, A. Buchleitner, Europhys. Lett. **46**, 24 (1999)
25. J.G. Leopold, I.C. Percival, Phys. Rev. Lett. **41**, 944 (1978)
26. I.C. Percival, Adv. Chem. Phys. **36**, 1 (1977)
27. A.J. Lichtenberg, M.A. Lieberman, *Regular and Stochastic Motion* (Springer-Verlag, New York, 1983)
28. V.N. Ostrovsky, N.V. Prudov, J. Phys. B **28**, 4435 (1995)
29. A. Buchleitner, D. Delande, Phys. Rev. A **55**, R1585 (1997)
30. K. Sacha, J. Zakrzewski, D. Delande, Eur. Phys. J. D **1**, 231 (1998)
31. J.B. Keller, Ann. Phys. (N.Y.) **4**, 180 (1958)
32. J. Müller, J. Burgdörfer, D. Noid, Phys. Rev. A **45**, 1471 (1992); J. Müller, J. Burgdörfer, Phys. Rev. Lett. **70**, 2375 (1993)
33. M. Domke *et al.*, Phys. Rev. A **53**, 1424 (1996); B. Püttner *et al.*, J. Electron. Spectrosc. Relat. Phenom. **101–103**, 27 (1999); B. Püttner *et al.*, Phys. Rev. Lett. **86**, 3747 (2001)
34. W.E. Cooke, T.F. Gallagher, Phys. Rev. Lett. **41**, 1648 (1978)
35. U. Eichmann, V. Lange, W. Sandner, Phys. Rev. Lett. **64**, 274 (1990)
36. P.M. Koch, Physica D **83**, 178 (1995)
37. B. Grémaud, D. Delande, Europhys. Lett. **40**, 363 (1997)
38. R. Grobe, J.H. Eberly, Phys. Rev. Lett. **68**, 2905 (1992)
39. R. Shakeshaft, Z. Phys. D **8**, 47 (1988)
40. C.L. Pekeris, Phys. Rev. **112**, 1649 (1958)
41. J.H. Shirley, Phys. Rev. **138**, B979 (1965)
42. Ya.B. Zel'dovich, Sov. Phys. JETP **24**, 1006 (1967)
43. U. Fano, Phys. Rev. **124**, 1866 (1961)
44. L.B. Madsen, P. Schlagheck, P. Lambropoulos, Phys. Rev. Lett. **85**, 42 (2000)
45. E. Balslev, J.M. Combes, Commun. Math. Phys. **22**, 280 (1971)
46. Y.K. Ho, Phys. Rep. **99**, 1 (1983)
47. W.P. Reinhardt, Ann. Rev. Phys. Chem. **33**, 223 (1982)
48. R. Blümel, U. Smilansky, Z. Phys. D **6**, 83 (1987)
49. M. Abramowitz, I.A. Stegun, *Handbook of Mathematical Functions*, 10th edn. (National Bureau of Standards, Washington, 1972), Chap. 22
50. D. Delande, A. Bommier, J.C. Gay, Phys. Rev. Lett. **66**, 141 (1991)
51. A. Buchleitner, B. Grémaud, D. Delande, J. Phys. B **27**, 2663 (1994)
52. R. Blümel, W.P. Reinhardt, in *Directions in Chaos*, edited by B.L. Hao *et al.* (World Scientific, Hong Kong, 1991), Vol. 4
53. H. Friedrich, *Theroretical Atomic Physics*, 2nd edn. (Springer, Berlin, 1998)
54. D. Lappas *et al.*, J. Phys. B **29**, L619 (1996)
55. K. Rzążewski, M. Lewenstein, P. Salières, Phys. Rev. A **49**, 1196 (1994)
56. F. Grossmann, T. Dittrich, P. Jung, P. Hänggi, Phys. Rev. Lett. **67**, 516 (1991)
57. H.P. Breuer, K. Dietz, M. Holthaus, Z. Phys. D **8**, 349 (1988)
58. O. Bohigas, S. Tomsovic, D. Ullmo, Phys. Rep. **223**, 43 (1993); S. Tomsovic, D. Ullmo, Phys. Rev. E **50**, 145 (1994)
59. K. Hornberger, A. Buchleitner, Europhys. Lett. **41**, 383 (1998)
60. O. Brodier, P. Schlagheck, D. Ullmo, Phys. Rev. Lett. **87**, 064101 (2001); Ann. Phys. (N.Y.) **300**, 88 (2002)